Swiss Accelerator Research and Technology

CHART Scientific Report

Thermo-Mechanical Behavior of an Alumina-Filled Paraffin Wax from Ambient to Cryogenic Temperatures. (MagComp3)

PSI:
Dr. Bernhard Auchmann, Dr. André Brem

CERN:
Dr. Roland Piccin

26.03.2026

1. Introduction / Original goals of this project

Recent advances in stress-managed asymmetric common-coils (SMACC) designs have re-opened the possibility of using wax-based systems.[1] Preliminary bonding experiments have demonstrated that wax-impregnated Nb_3Sn Rutherford cables can function effectively in background magnets field, reaching the critical current without a single quench during training cycles [2] and extending to other magnet designs.[3] Overall, any next-generation impregnation material must be rigorously validated against the stringent requirements outlined above, under the extreme service conditions of cryogenics temperatures, high Lorentz force and radiation exposure.

In this study, the thermo-mechanical properties of an alumina-filled wax system (developed by PSI [4] are examined and characterized as a candidate next-generation impregnation material for high-field superconducting magnets operating at cryogenic temperatures. Section~2 describes the materials and experimental methodology. The corresponding results, the microstructure–property relationships and underlying damage mechanisms and the main conclusions are summarized in Section~3.

2. Realisation

Materials

The “pure wax” system consists of fully refined paraffin wax (Polarit G 54/56, Deffner & Johann GmbH) and carnauba wax (grade 1, Sigma-Aldrich) used as a dispersant at 10 wt.%. The “filled wax” system was obtained by adding sub-micrometer alumina (Al2O3) particles (PB4 MAR alpha-alumina, Baikowski) to the pure wax system.

The dispersion process of the filled wax was carried out as follows: (1) both waxes were mixed under stirring at 90 °C; (2) the mixture was degassed at 1 mbar until bubble evolution became negligible; (3) preheated alumina powder (90 °C) was added under magnetic stirring; (4) high-shear mixing was applied until a cream-like consistency was obtained without visible agglomerates; and (5) the mixture was degassed again under continuous stirring at 90 °C and 1 mbar.[4]

All sample geometries were cut by water jet from molded plates prepared using two parallel polymethylmethacrylate plates separated by metallic spacer bars.

Table 1. Concentration of each component in pure wax and filled wax in volume and weight fractions at room temperature.

Component	Pure wax vol.%	Pure wax wt.%	Filled wax vol.%	Filled wax wt.%
Paraffin wax	90.9	90.1	50	19.7
Carnauba wax	9.1	9.9	5	2.2
Alumina	–	–	45	78.1

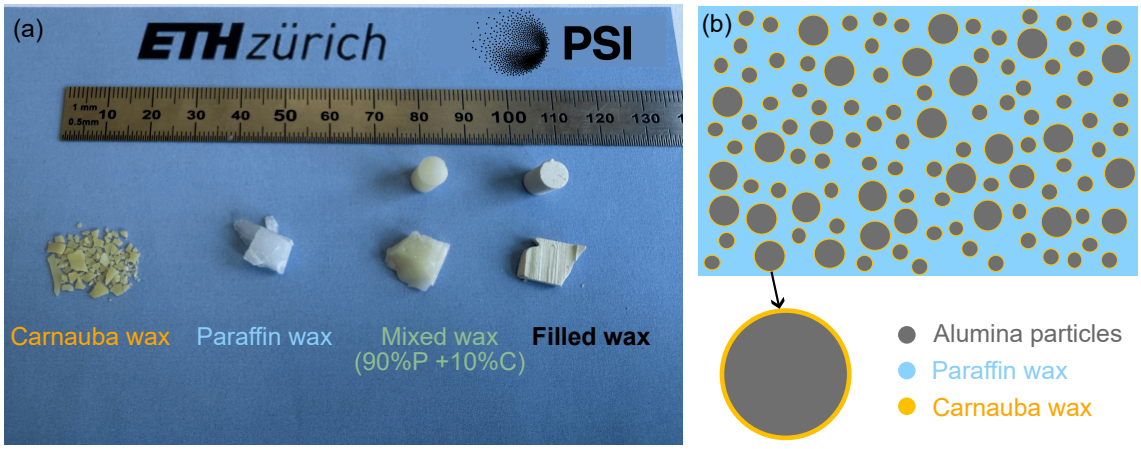

Figure 1. (a) The four material systems examined in this study: carnauba wax, paraffin wax, pure (mixed) wax, and filled wax. (b) Schematic illustration of the alumina-filled wax system.

Differential scanning calorimetry (DSC)

Differential scanning calorimetry was conducted using a TA Instruments DSC2500 calibrated with indium. Samples of approximately 3 mg were heated under nitrogen. Thermal properties, including melting and crystallization temperatures, were determined using the following program: heating from 5 °C to 100 °C at 5 °C/min, an isothermal hold at 100 °C for 10 min,

cooling to 5 °C at 5 °C/min, and an isothermal hold at 5 °C for 20 s. This cycle was performed twice, with the first run used to erase thermal history and the second used for analysis.

Thermogravimetric analysis (TGA)

Thermogravimetric analysis was performed on a TA Instruments TGA5500 in air and nitrogen to quantify mass loss due to evaporation and thermal degradation of the wax phase. Samples of 7–10 mg were heated from 25 °C to 700 °C at 5 °C/min under a gas flow of 25 mL/min.

Thermal contraction analysis

Rectangular specimens (55 × 12.6 × 2.5 mm) of both filled wax and pure wax were prepared to measure thermal contraction and determine the coefficient of thermal expansion. The sample surfaces were coated with a stochastic speckle pattern and monitored in a temperature-controlled oven using digital image correlation. Cooling was conducted from room temperature down to −80 °C (193 K) at 2 °C/min. For liquid-nitrogen measurements, specimens were immersed in LN2 for at least 10 min and imaged through a circular viewing window.

Dynamic viscosity

Rheological measurements were performed using an Anton Paar MCR 302e rheometer. Steady-shear tests were conducted at shear rates from 100 s^{-1} down to 0.1 s^{-1} using helical impeller and vane spindle geometries. Prior to measurement, the melts were maintained at 110 °C, degassed under stirring, and poured into a metallic cylindrical container. The materials were equilibrated under steady shear at 100 s^{-1} before testing.

Dynamic mechanical thermal analysis (DMTA)

DMTA was carried out in three-point bending on a TA Instruments Ares-G2 instrument equipped with a forced-convection oven cooled by liquid nitrogen flow. Beam specimens were 9.5 mm wide and 4 mm thick with a support span of 40 mm. A sinusoidal oscillation of 5 µm amplitude at 1 Hz was applied with a preload of 5 N while the temperature was ramped from −130 °C to 35 °C at 2 °C/min.

Uniaxial compression testing

Compressive experiments were performed using a ZwickRoell Z050 AllroundLine universal testing machine equipped with a 50 kN load cell. A temperature-controlled oven provided temperatures from 250 °C down to −80 °C (193 K). Cylindrical specimens with a diameter of 6 mm and height of 7 mm were tested at Hencky strain rates between 10^{-4} s^{-1} and 10^{-1} s^{-1}. For cryogenic measurements, specimens were fully immersed in a liquid-nitrogen bath and tested after thermal equilibrium had been reached.

Fracture toughness testing

Fracture toughness tests were performed on the same testing machine using a 200 N load cell. Single-edge notched bending specimens were prepared according to ASTM D5045-14 to evaluate plane-strain fracture toughness K_{Ic} from room temperature down to cryogenic temperatures. The support span was 32 mm with cylindrical rollers of 5 mm diameter, and the crosshead displacement rate was 2 mm/min.

Gel permeation chromatography (GPC)

High-temperature size exclusion chromatography was used to characterize the molar mass distribution of the wax components. Measurements were performed on an Agilent 1260 Infinity II HPLC system equipped with two PSS POLEFIN analytical XL columns. Samples were eluted with 1,2,4-trichlorobenzene at 150 °C and a flow rate of 1.0 mL/min, with calibration using polystyrene standards.

Scanning electron microscopy (SEM)

Microscopy imaging was performed using a ZEISS GeminiSEM 450. Samples were mounted on aluminum stubs using conductive carbon tape and sputter-coated with a thin platinum layer to minimize charging.

3. Results / Conclusions / Deliverables

Molecular weight distribution

The molecular weight distributions of pure wax, paraffin wax, and carnauba wax show peak molar masses of 586, 553, and 1711 g/mol, respectively. The pure wax displays one dominant peak originating from the 90% paraffin fraction and a smaller peak associated with the 10% carnauba fraction. The natural carnauba wax exhibits two distinct peaks, consistent with its composition as a complex mixture of long-chain esters and hydrocarbons.

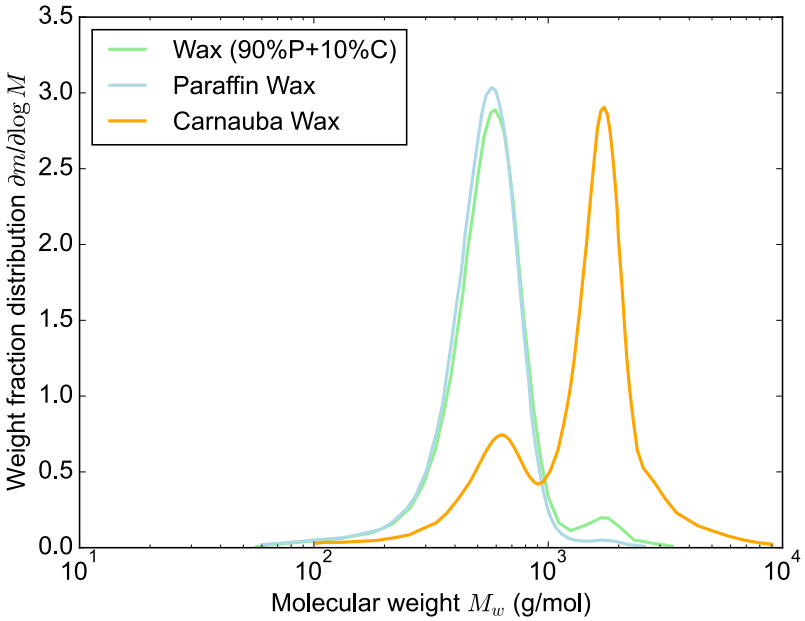

Figure 2. Molecular weight distribution of the pure wax (light green), paraffin wax (light blue) and carnauba wax (orange).

Table 2. Molecular weight summary of wax systems: summary of number-average (Mn), weight-average (Mw), peak molar masses (Mp), and polydispersity index (Đ) of the pure wax (90% paraffin + 10% carnauba), paraffin wax, and carnauba wax.

	Pure wax	Paraffin wax	Carnauba wax
Mn (g/mol)	486	468	1017
Mw (g/mol)	616	558	1587
Mp (g/mol)	586	553	1711
Đ (-)	1.3	1.2	1.6

DSC results

The paraffin–carnauba wax system shows eutectic phase behavior with a strong melting-point depression of the carnauba phase as paraffin content increases. This behavior indicates full miscibility of the two components in the liquid state. Cooling and heating curves of the filled wax system show that inert alumina does not alter the phase behavior of the wax mixture; the key thermal transitions remain at essentially the same temperatures as in the unfilled system.

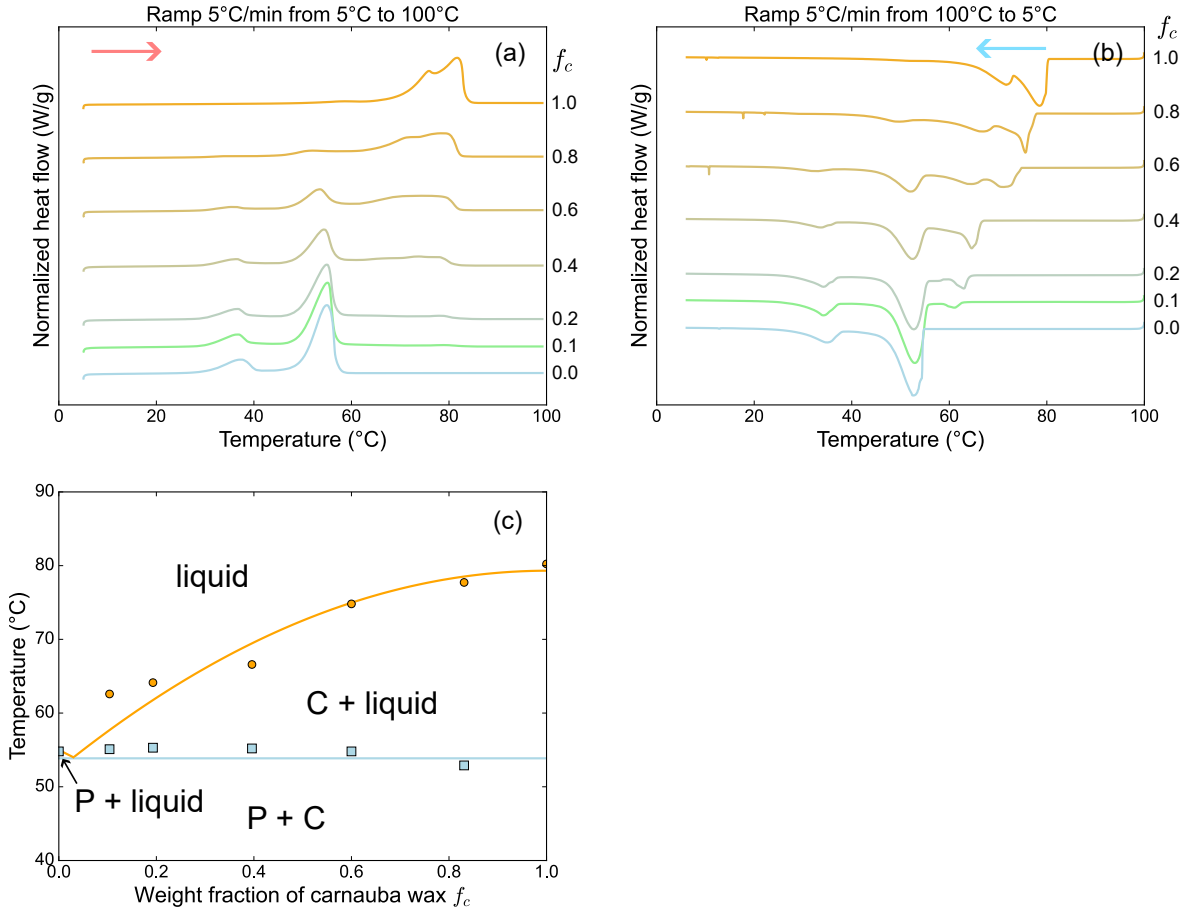

Figure 3. DSC thermograms of paraffin–carnauba wax mixtures for various weight fractions of carnauba wax f_c: (a) heating and (b) cooling cycles. (c) The corresponding phase diagram as a function of f_c. The solid lines are guides to the eye.

TGA results

TGA results show that the onset of 1% mass loss for the filled wax occurs at about 188 °C in air, compared with about 180 °C for pure wax and paraffin wax, while carnauba wax shows the highest thermal stability. Under nitrogen, degradation is shifted to higher temperatures

for all systems. The residual mass of the filled wax at 700 °C matches the nominal alumina content very well.

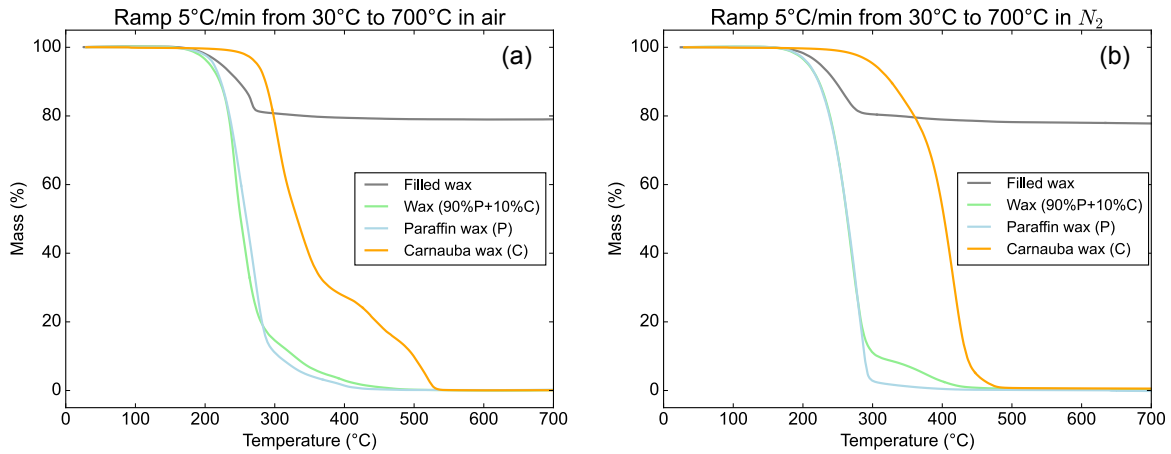

Figure 4. Thermogravimetric analysis (TGA) of the filled wax, pure wax, paraffin wax, and carnauba wax: mass fraction as a function of temperature under (a) air and (b) nitrogen flow, measured at a heating rate of 5 °C/min.

Thermal contraction tests

The addition of 45 vol.% alumina reduces overall thermal shrinkage by nearly half, from 1.48% for pure wax to 0.79% from room temperature to 193 K. The filled wax exhibits CTE values of 104.6 × 10^{-6} K^{-1} from room temperature to 260 K and 67.6 × 10^{-6} K^{-1} from 260 K to 193 K. For pure wax, the corresponding values are 190.4 × 10^{-6} K^{-1} and 121.9 × 10^{-6} K^{-1}. The pure wax showed irregular surface cracking under thermal shock, whereas no macroscopic cracks were observed in the filled wax.

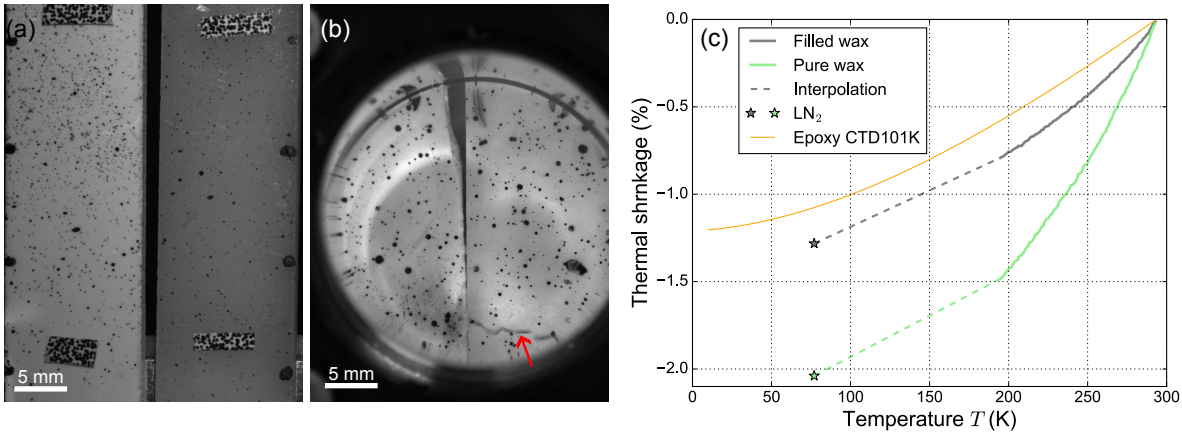

Figure 5. Thermal contraction tests of (a-b) filled wax (left) and pure wax (right) at (a) RT and at (b) LN2. (c)~Thermal shrinkage (%) as a function of temperature from -80°C to RT at 2°C/min, and at LN_2 (star). Orange line: epoxy CTD101K [5].

Rheological properties

The pure wax behaves as a Newtonian fluid with a low steady-state shear viscosity at high temperature. The filled wax exhibits a much higher viscosity but remains processable, with shear-thinning behavior characteristic of densely packed rigid particles in a wax matrix. Even at a low shear rate of 1 s^{-1}, the viscosity remained below 1000 mPa·s, which is compatible with vacuum impregnation.

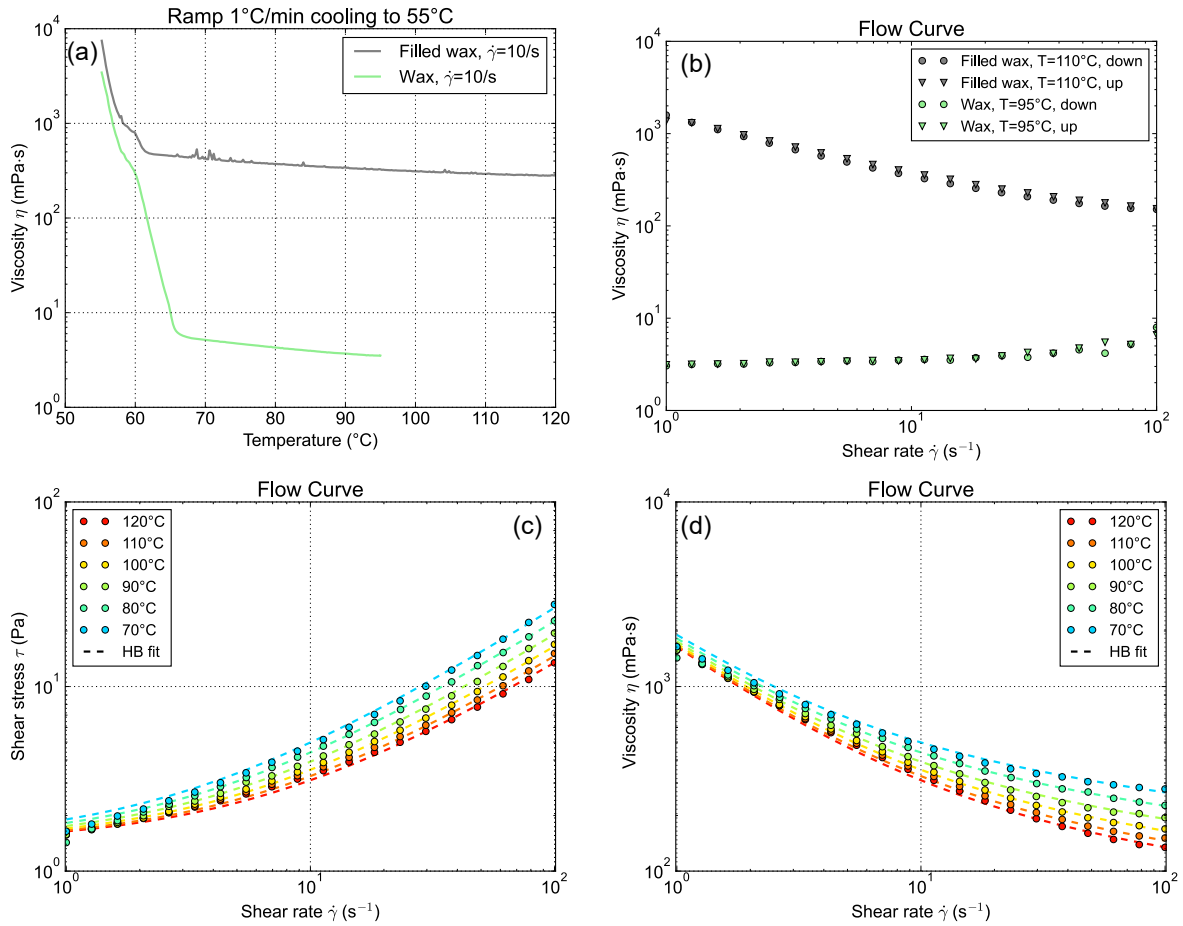

Figure 6. Rheological characterization of the pure wax and filled wax usingimpeller geometry under steady shear: (a) Viscosity during cooling at a ramp of 1 °C/min. (b) Flow curves measured by sweeping the shear rate from 1/s to 100/s (up) and from 100/s to 1/s (down). The flow curves of filled wax in terms of (c) shear stress τ and (d) shear viscosity η from 120 °C to 70 °C at an decreasing shear-rate ramp from 100/s to 1/s.

Uniaxial compression results

As temperature decreases, both materials show increased compressive strength and reduced ductility. At 193 K, the filled wax reaches an average compressive strength of 54.4 MPa versus 27.6 MPa for pure wax. At liquid-nitrogen temperature, the filled wax reaches 80.9 MPa, whereas pure-wax specimens crack during cooling and could not be tested reliably. The yield stress of the filled wax is roughly three times that of pure wax at room temperature and shows clear temperature dependence but limited strain-rate dependence at cryogenic conditions.

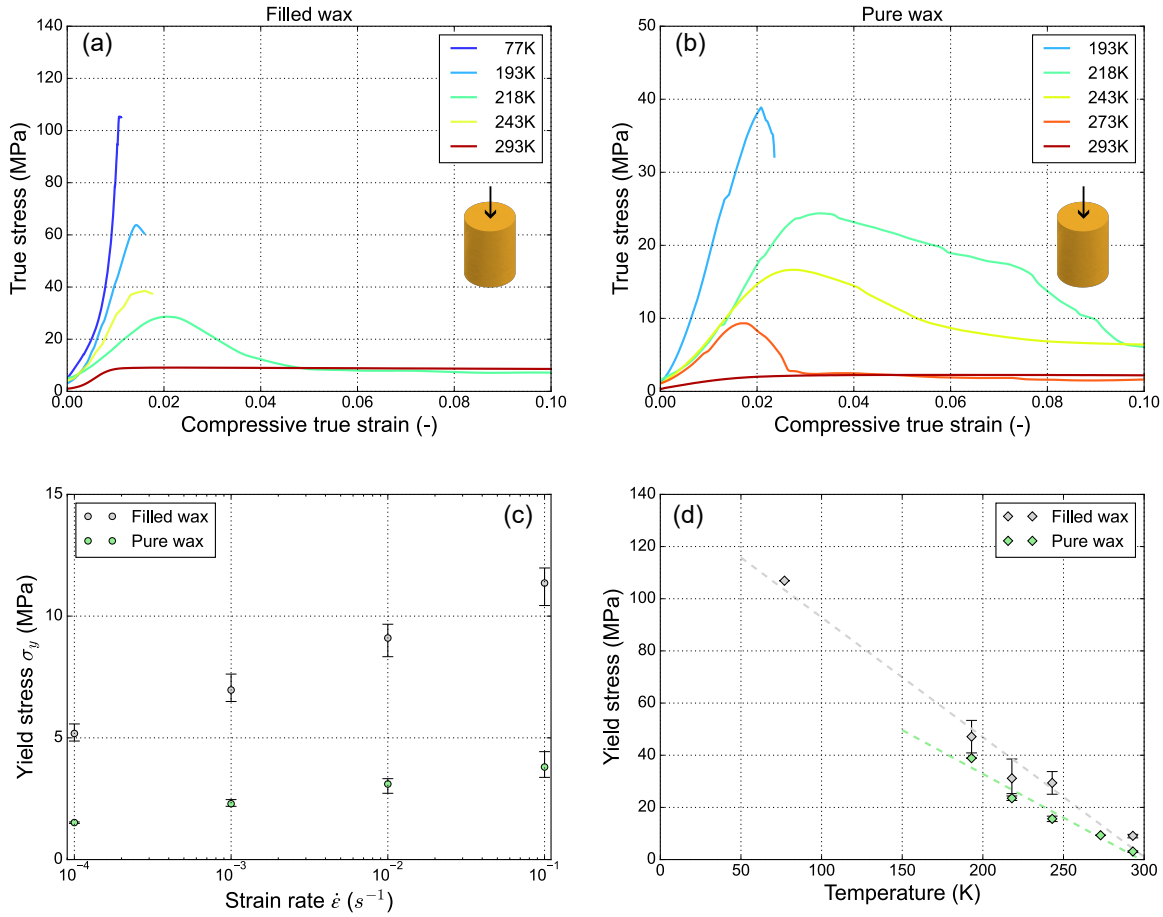

Figure 7. Uniaxial compression results for (a) the filled wax and (b) the pure wax at various temperatures, tested at a strain rate $\dot{\varepsilon} = 1 \cdot 10^{-2}/s$. (c) Strain- rate dependence of the yield stress σy for both materials at room temperature (293 K). (d) Yield stress σy as a function of temperature for both material systems at $\dot{\varepsilon} = 1 \cdot 10^{-2}/s$.

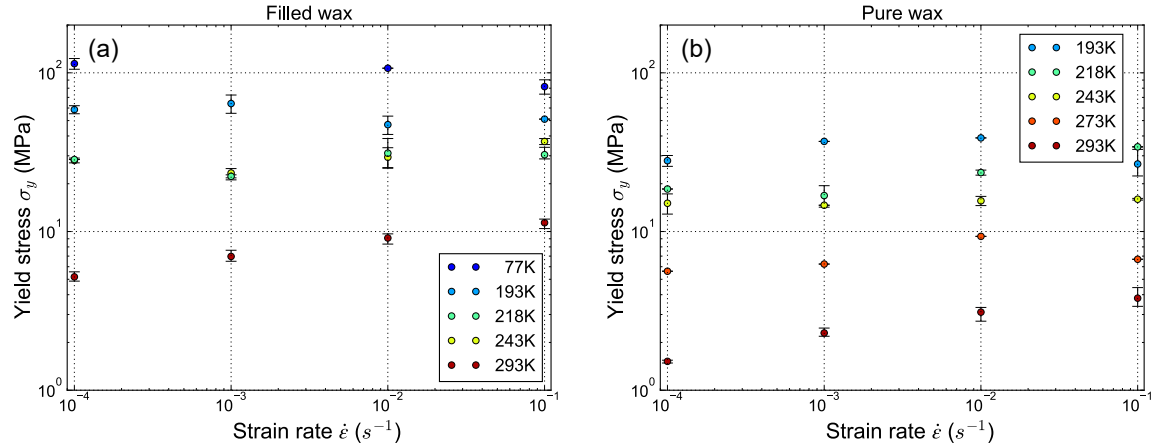

Figure 8. The curves of compressive yield stress versus strain rate for the (a) filled wax and (b) pure wax from ambient to cryogenic temperatures.

Dynamic properties of 3-point bending

At 1 Hz, the storage modulus of the filled wax is about 4.9 GPa at room temperature and rises to 17.9 GPa at −130 °C. A clear β-transition is visible near −65 °C (208 K) in the loss tangent. Extrapolation predicts a modulus of about 20.2 GPa at 77 K, which is substantially higher than that of a conventional rigid epoxy resin.

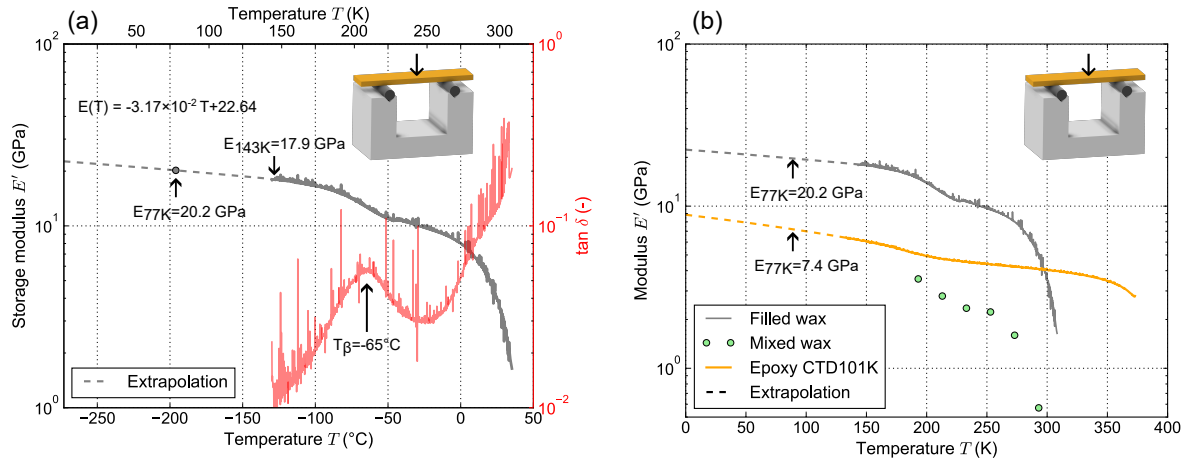

Figure 9. (a) Dynamic 3-point bending results obtained at a frequency of 1 Hz: storage modulus E′ and loss tangent tan δ as functions of temperature during heating from −130 °C to 35 °C at a rate of 2 °C/min. (b) Comparison of the modulus of the filled wax with that of a conventional epoxy resin and the pure-wax system.

Linear fracture mechanics

At room temperature, the addition of alumina raises the fracture toughness from 0.127 to 0.525 MPa·√m. At 193 K, however, the fracture toughness of the filled wax decreases to 0.246 MPa·√m, indicating that thermal mismatch stresses between the alumina particles and wax matrix reduce fracture resistance at cryogenic temperatures. LN2 exposure causes irreversible thermal-shrinkage-induced damage, further reducing fracture toughness.

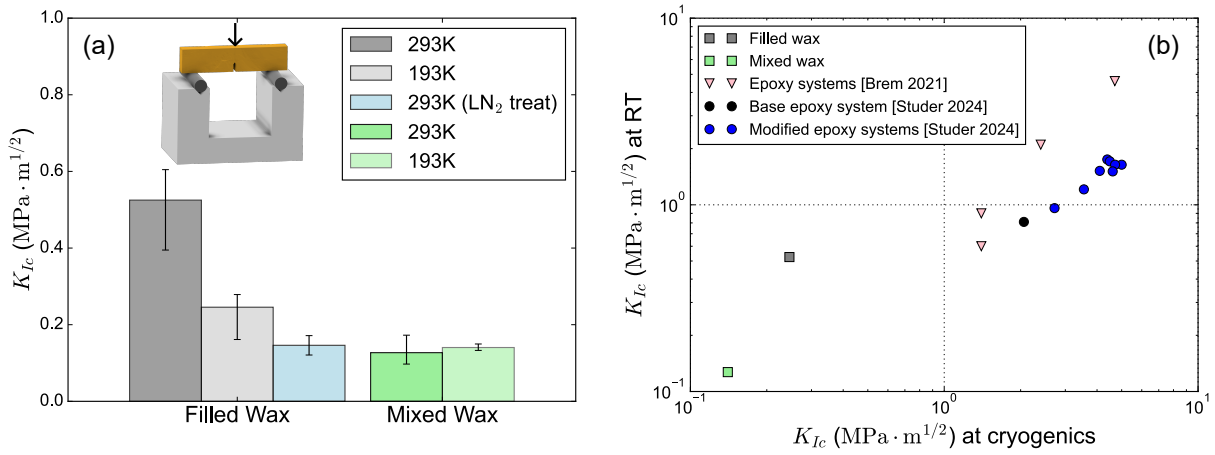

Figure 10. (a) Experimental plane-strain fracture toughness KIc of the filled wax and pure wax at room temperature and 193 K. (b) Reference fracture-toughness values of epoxy resin systems [12, 31] measured at room temperature and liquid-nitrogen (LN2) temperature.

Table 2. Summary of thermal properties of filled wax, pure wax, paraffin wax, and carnauba wax.

Property	Filled wax	Pure wax	P-wax	C-wax
Solid transition peak (°C)	35.9	35.1	37.2	62.1
Melting onset (°C)	46.5	46.3	49.8	70.6
Melting peak (°C)	54.1	54.4	54.9	81.6
Melting endset (°C)	55.6	56.0	56.8	83.3
Recrystallization peak (°C)	52.8, 61.9	52.3, 60.7	52.7	78.5
Degradation onset in air (°C)	188.3	179.5	180.2	243.1
Degradation onset in N2 (°C)	190.3	180.0	182.1	250.9
CTE (10^-6 K^-1)	104.6–67.6	190.4–121.9	–	–

Table 3. Summary of mechanical properties of pure wax and filled wax.

Property	Wax RT	Wax cold	Filled wax RT	Filled wax cold
Bending modulus (GPa)	0.6	3.6 (193 K)	4.9	17.8 (173 K)
Yield stress (compression) (MPa)	2.75	27.62 (193 K)	8.15	80.91 (LN2)
Fracture toughness (MPa·√m)	0.127	0.140 (193 K)	0.525	0.246 (193 K)
Dynamic viscosity (mPa·s)	3.5–6.2	—	282–478	—

Damage Mechanism

The cryo-mechanical experiments involve two sequential stages: cooling from room temperature to cryogenic conditions, during which significant thermal stresses develop, followed by mechanical testing at low temperature.

Although the filled wax exhibits a reduced macroscopic coefficient of thermal expansion (CTE) of about $100 \cdot 10^{-6}$ K^{-1} (see Figure 5), a strong mismatch persists at the microscale between the high-CTE wax matrix and the low-CTE alumina particles ($5.4 \cdot 10^{-6}$ K^{-1} [6]). Upon cooling, this mismatch induces local tensile strains in the matrix, as its contraction is constrained by the rigid particles, leading to internal stress buildup.

SEM images reveal a densely packed and well-dispersed particle network, where the wax acts as a binder between alumina particles ranging from sub-micrometer clusters down to a few hundred nanometers. Quantifying the resulting thermal stresses is therefore essential for understanding the mechanical response prior to cryogenic testing.

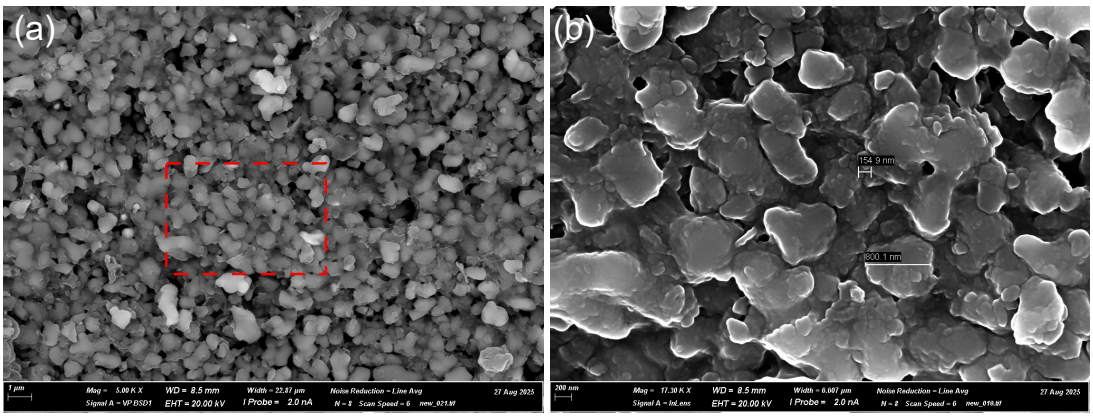

Figure 11. SEM images of undeformed filled wax containing alumina particles at a volume fraction of Vp = 45%, well dispersed within the wax matrix at room temperature. (b) Zoomed-in view of the region highlighted in (a).

A two-dimensional representative volume element (RVE) with randomly distributed alumina particles (45 vol%) was simulated using ANSYS under plane strain conditions. Cooling from 328 K to 77 K induces thermal mismatch strains due to the large CTE difference between wax and alumina, followed by an additional 3% compressive loading at 77 K.

Cooling generates localized plastic strains (~10%) and tensile stresses (up to ~70 MPa) in narrow wax ligaments between particles, indicating significant pre-damage before mechanical loading. Under compression, strain localizes further (>20%), while tensile stress pockets persist near particle interfaces. These regions act as initiation sites for interfacial debonding and crack formation.

As a result, failure in the filled wax is governed by tensile stress localization at particle–matrix interfaces, leading to cracks perpendicular to the loading direction, rather than shear-dominated failure observed in pure wax.

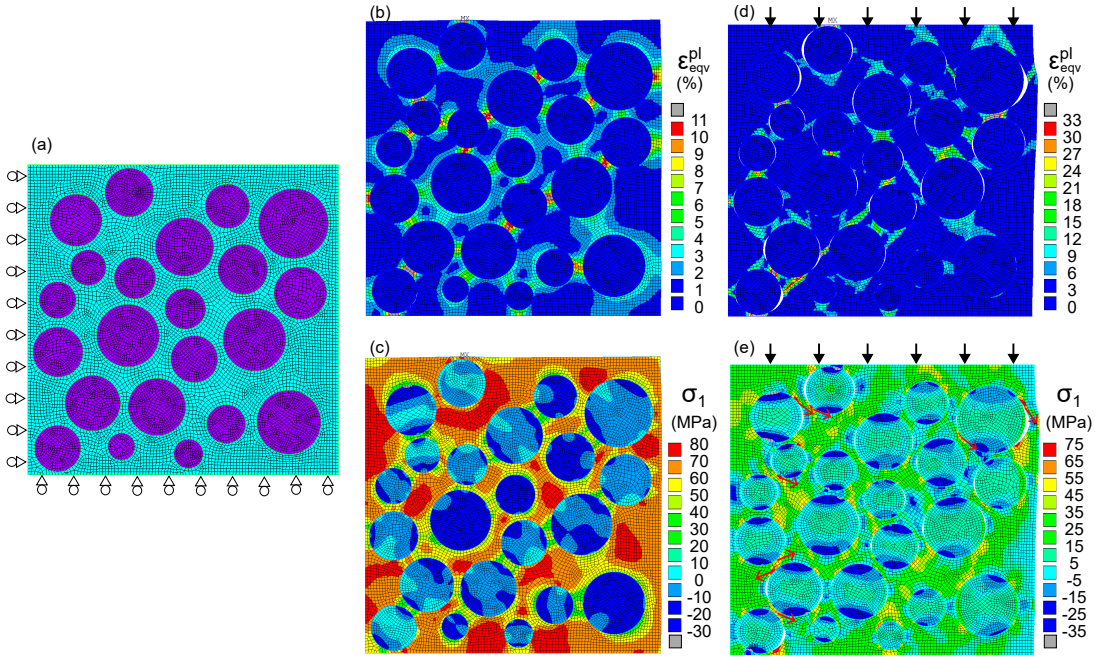

Figure 12. R VE model with a particle volume fraction of V_p = 45% embedded in the wax matrix (light blue). (a) Initial configuration. (b–c) Equivalent plastic strain $\varepsilon^{pl}{}_{eqv}$ and principal stress σ_1 fields after thermal cooling from 328 K to 77 K. (d–e) Corresponding $\varepsilon^{pl}{}_{eqv}$ and σ_1 fields under an additional 3 % compressive strain applied at 77 K. Here the principal stress directions are indicated by red arrows.

Conclusions

A paraffin–carnauba wax system filled with 45 vol% sub-micrometer alumina particles was characterized from room temperature to cryogenic conditions. The composite combines low melt viscosity with reduced thermal contraction and significantly improved mechanical performance, making it a promising impregnation material for high-field superconducting magnets.

The wax mixture exhibits typical eutectic behavior, while alumina addition does not affect melting or crystallization; the system remains thermally stable up to ~190 °C. Due to the low CTE of alumina, thermal contraction is reduced by about a factor of two, improving compatibility with metallic components and reducing thermal stresses.

Despite high filler content, the melt viscosity remains sufficiently low for impregnation and shows shear-thinning behavior. Mechanically, the filled wax exhibits strongly enhanced stiffness and strength, reaching ~5 GPa at room temperature and >18 GPa at cryogenic temperatures, with compressive strength exceeding 80 MPa at LN_2.

Fracture toughness increases at room temperature but decreases at low temperature due to thermal mismatch-induced damage. Nevertheless, the combination of moderate toughness, low adhesion, and low energy release remains beneficial for quench mitigation.

RVE simulations reproduce the development of thermal mismatch stresses and strain localization, providing insight into damage mechanisms and guiding microstructural optimization.

4. Publications and Outreach

- X. Kong, J. L. Van Den Eijnden, A. Brem, D. Araujo, B. Auchmann, T. A. Tervoort, Light a candle for impregnation of superconducting magnets with wax: Thermo-mechanical behavior of an alumina-filled paraffin wax from ambient to cryogenic temperatures, *Cryogenics*, 2026, 157, 104326.
- X. Kong, Recent results of an alumina-filled paraffin wax system for Nb3Sn coil composites, HFM annual meeting 2026, CERN Geneva Switzerland.
- X. Kong, Mechanical Modelling and Failure Identification of Impregnated Nb3Sn Rutherford cable stacks. CHART Workshop 2025, PSI, Villigen Switzerland.
- X. Kong, Characterization and modeling of temperature- and rate-dependent mechanical behaviors applied to an epoxy resin from room to cryogenic temperatures, 12th European Solid Mechanics Conference (ESMC2025), 6 - 11 July, Lyon, France.
- X. Kong, Mechanical identification and modelling of impregnated Nb3Sn Rutherford cable stacks under compressive loading, HFM annual meeting 2025, CERN, Geneva, Switzerland.

5. References

[1] D. M. Araujo, B. Auchmann, A. Brem, M. Daly, T. Michlmayr, C. Müller, H. Garcia-Rodrigues, D. Sotnikov, A. Milanese, Subscale Stress-Managed Common Coil Design, *IEEE Transactions on Applied Superconductivity*, 2024, 34, 1–5.

[2] M. Daly, B. Auchmann, C. Hug, S. Sidorov, S. Otten, A. Kario, M. Dhallé, H. Ten Kate, BOX: an efficient benchmark facility for the study and mitigation of interface-induced training in accelerator type high-field superconducting magnets, *Superconductor Science and Technology*, 2021, 34, 115008.

[3] B. Auchmann, D. M. Araujo, A. Brem, M. Daly, R. Felder, J. Feuvrier, C. Hug, O. Kirby, F. Mangiarotti, A. Milanese, G. Montenero, G. Rolando, S. Sanfilippo, S. Sidorov, Test Results From CD1 Short CCT Nb$_{3}$Sn Dipole Demonstrator and Considerations About CCT Technology for the FCC-Hh Main Dipole, *IEEE Transactions on Applied Superconductivity*, 2024, 34, 1–6.

[4] A. Brem, M. Duda, C. Müller, H. Garcia, C. Hug, M. Daly, D. Martins Araujo, J. Kosse, S. Otten, A. Kario, H. H. J. T. Kate, A. Milanese, B. Auchmann, From Hot to Cold: Advanced Materials and Processes for NbSn Based Magnets <sub/>, *IEEE Transactions on Applied Superconductivity*, 2024, 34, 1–5.

[5] G. Kirby, V. I. Datskov, S. Clement, A. Chiuchiolo, P. Fessia, G. Gauthier, G. Lynch, J. Murtomaki, J. Van Nugteren, F.-O. Pincot, J. C. Perez, G. Rossi, G. De Rijk, S. Tavares, V. Venturi, Thermal Contraction: Experimental Data and Fits for the Thermal Contraction of Future Magnet Materials at Cryo- genic Temperatures,, , 2016, .

[6] J. W. Ekin, Experimental Techniques for Low-Temperature Measurements, Oxford University Press, Oxford, UK, 2006.